Using internal strain and mass to modulate Dy⋯Dy coupling and relaxation of magnetization in heterobimetallic metallofullerenes DyM₂N@C₈₀ and Dy₂MN@C₈₀ (M = Sc, Y, La, Lu)

Yajuan Hao,[a,b] Georgios Velkos,[a] Sandra Schiemenz,[a] Marco Rosenkranz,[a] Yaofeng Wang,[a] Bernd Büchner,[a] Stanislav M. Avdoshenko,*[a] Alexey A. Popov,*[a] Fupin Liu*[a]

Supporting Information

Experimental details

X-ray diffraction. Single crystal X-ray diffraction data collection was carried out at 100 K at the BESSY storage ring (BL14.2, Berlin-Adlershof, Germany).[1] XDSAPP2.0 suite was employed for data processing.[2, 3] The structure was solved by direct methods and refined by SHELXL-2018.[4] Hydrogen atoms were added geometrically and refined with a riding model.

Mass spectrometry: Laser desorption/ionization time-of-flight (LDI-TOF) mass-spectra were measured with a Bruker autoflex mass-spectrometer.

UV-Vis spectrometry: UV-vis-NIR absorption spectra were measured in toluene solution at room temperature with Shimadzu 3100 spectrophotometer.

IR spectrometry: IR spectra were measured in transmission mode using Hyperion FTIR microscope attached to Vertex 80 FTIR spectrometer (Bruker). Samples were drop-casted on KBr single-crystalline substrate and dried under vacuum.

Magnetic measurements. DC and AC magnetic measurements of powder samples were performed using a Quantum Design VSM MPMS3 magnetometer. Magnetic simulations and fitting were performed using PHI code.[5]

DFT computation. DFT optimization of $M_3N@C_{80}$ molecules was performed in Ref. [6] at the PBE-D/PAW level using the VASP code and recommended pseudopotentials with f-shell in-core treatment.[7-11]

CASSCF calculations. *Ab initio* energies and wave functions of Dy^{3+} LF multiplets in $M_3N@C_{80}$ molecules have been calculated at the CASSCF/SO-RASSI level of theory using the quantum chemistry package OpenMOLCAS.[12] The single ion LF-parameters were calculated based on *ab initio* data with the use of SINGLE_ANISO module.[13]

Spectroscopic characterization
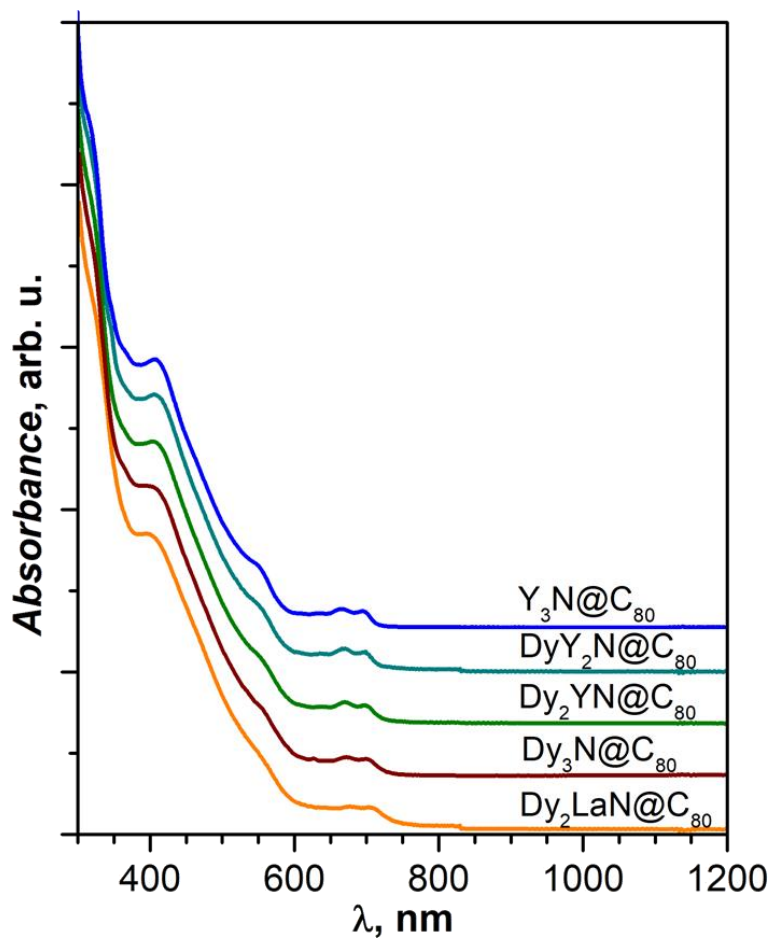
Figure S1. UV-Vis-NIR absorption spectra of Dy$_x$Y$_{3-x}$N@I_h-C$_{80}$ (x = 0–3) and Dy$_2$LaN@I_h-C$_{80}$ in toluene solution.
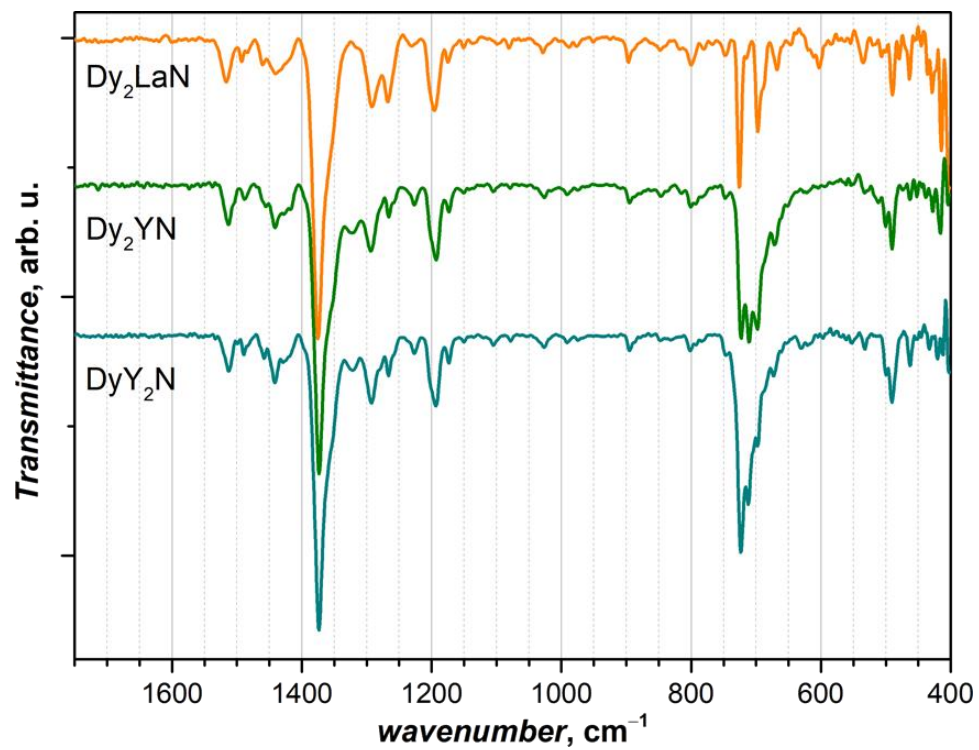
Figure S2. FT-IR absorption spectra of $Dy_2LaN@I_h$-C_{80}, $Dy_2YN@I_h$-C_{80}, and $DyY_2N@I_h$-C_{80}.

Table S1. Crystal data for Dy$_x$Y$_{3-x}$N@C$_{80}$

Crystal	Dy$_3$N@C$_{80}$·NiOEP·2(C$_6$H$_6$)	Dy$_2$YN@C$_{80}$·NiOEP·2(C$_6$H$_6$)
Formula	C$_{128}$H$_{56}$Dy$_3$N$_5$Ni	C$_{128}$H$_{56}$Dy$_{2.37}$N$_5$Ni
Formula weight	2209.98	2107.61
Color, habit	Black, block	Black, block
Crystal system	monoclinic	triclinic
Space group	$C2/c$	$P\bar{1}$
a, Å	25.260(5)	14.680(3)
b, Å	15.050(3)	15.420(3)
c, Å	39.490(8)	17.700(4)
α, deg	90	81.15(3)
β, deg	95.39(3)	74.44(3)
γ, deg	90	86.41(3)
Volume, Å^3	14946(5)	3812.9(15)
Z	8	2
T, K	100	100
Radiation (λ, Å)	Synchrotron Radiation (0.77977)	Synchrotron Radiation (0.77977)
Unique data (R_{int})	23501 (0.0806)	22329 (0.0749)
Parameters	1299	1325
Restraints	19	864
Observed data ($I > 2\sigma(I)$)	22966	20633
Goodness-of-fit on F^2	1.029	1.036
ρ_{calc}, g/cm^3	1.964	1.836
$R_1{}^a$ (observed data)	0.0537	0.0884
$wR_2{}^b$ (all data)	0.1489	0.2455
CCDC NO.	2184669	2184670

[a]For data with $I > 2\sigma(I)$, $R_1 = \dfrac{\sum||F_o|-|F_c||}{\sum|F_o|}$. [b]For all data, $wR_2 = \sqrt{\dfrac{\sum\left[w\left(F_o^2-F_c^2\right)^2\right]}{\sum\left[w\left(F_o^2\right)^2\right]}}$.

Table S1 (continued). Crystal data for Dy$_x$Y$_{3-x}$N@C$_{80}$

Crystal	DyY$_2$N@C$_{80}$ · NiOEP · 2(C$_6$H$_6$)	Y$_3$N@C$_{80}$ · NiOEP · 2(C$_6$H$_6$)
Formula	C$_{128}$H$_{56}$Dy$_{1.95}$N$_5$Ni	C$_{128}$H$_{56}$N$_5$NiY$_3$
Formula weight	2039.16	1989.21
Color, habit	Black, block	Black, block
Crystal system	monoclinic	monoclinic
Space group	C2/c	C2/c
a, Å	25.290(5)	25.270(5)
b, Å	15.060(3)	15.070(3)
c, Å	39.420(8)	39.470(8)
α, deg	90	90
β, deg	95.28(3)	95.22(3)
γ, deg	90	90
Volume, Å³	14950(5)	14969(5)
Z	8	8
T, K	100	100
Radiation (λ, Å)	Synchrotron Radiation (0.77977)	Synchrotron Radiation (0.77977)
Unique data (R_{int})	24172 (0.1136)	25477 (0.0630)
Parameters	1275	1272
Restraints	24	18
Observed data ($I > 2\sigma(I)$)	22939	18407
Goodness-of-fit on F^2	1.051	1.041
ρ$_{calc}$, g/cm³	1.812	1.765
$R_1{}^a$ (observed data)	0.0563	0.0753
$wR_2{}^b$ (all data)	0.1577	0.2285
CCDC NO.	2184671	2184672

[a]For data with $I > 2\sigma(I)$, $R_1 = \dfrac{\sum \lVert F_o \rvert - \lvert F_c \rVert}{\sum \lvert F_o \rvert}$. [b]For all data, $wR_2 = \sqrt{\dfrac{\sum\left[w\left(F_o^2 - F_c^2\right)^2 \right]}{\sum\left[w\left(F_o^2\right)^2 \right]}}$.

Table S2. Crystal data for $Dy_2LaN@C_{80}$.

Crystal	$LaDy_2N@C_{80} \cdot NiOEP \cdot 2C_6H_6$
Formula	$C_{128} H_{56} Dy_{2.45} N_5 Ni$
Formula weight	2121.22
Color, habit	Black, block
Crystal system	monoclinic
Space group	$C2/c$
a, Å	25.270(5)
b, Å	15.080(3)
c, Å	39.460(8)
α, deg	90
β, deg	95.31(3)
γ, deg	90
Volume, Å³	14973(5)
Z	8
T, K	100
Radiation (λ, Å)	Synchrotron Radiation (0.77977)
Unique data (R_{int})	22315 (0.0477)
Parameters	2066
Restraints	2172
Observed data ($I > 2\sigma(I)$)	17085
Goodness-of-fit on F^2	1.025
ρ_{calc}, g/cm³	1.882
$R_1{}^a$ (observed data)	0.0486
$wR_2{}^b$ (all data)	0.1557
CCDC NO.	2184673

[a]For data with $I > 2\sigma(I)$, $R_1 = \dfrac{\sum||F_o|-|F_c||}{\sum|F_o|}$. [b]For all data, $wR_2 = \sqrt{\dfrac{\sum\left[w\left(F_o^2-F_c^2\right)^2\right]}{\sum\left[w\left(F_o^2\right)^2\right]}}$.
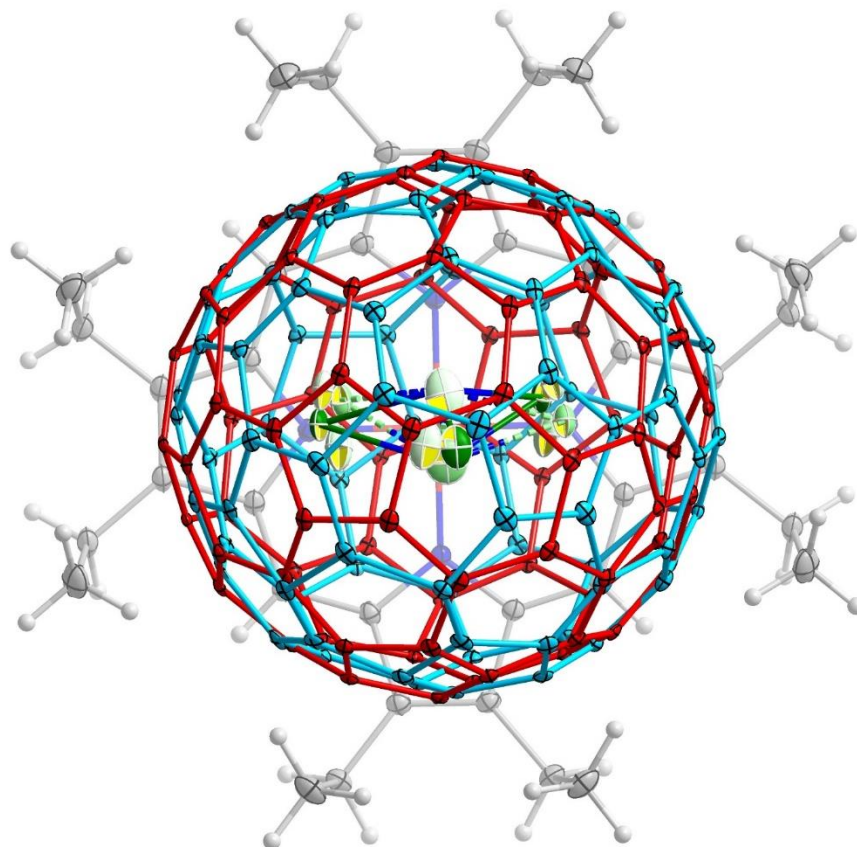
Figure S3. Single-crystal X-ray structures of LaDy$_2$N@C$_{80}$·NiOEP·2C$_6$H$_6$. To show the relation between two C$_{80}$ orientations, the structure is viewed perpendicular to the NiOEP. The displacement parameters are shown at the 30% probability except for those of cage carbons, which are shown at the 5% probability to highlight the orientations. Colour code: grey for carbon, blue for nitrogen, white for hydrogen, red for nickel, and green for dysprosium.
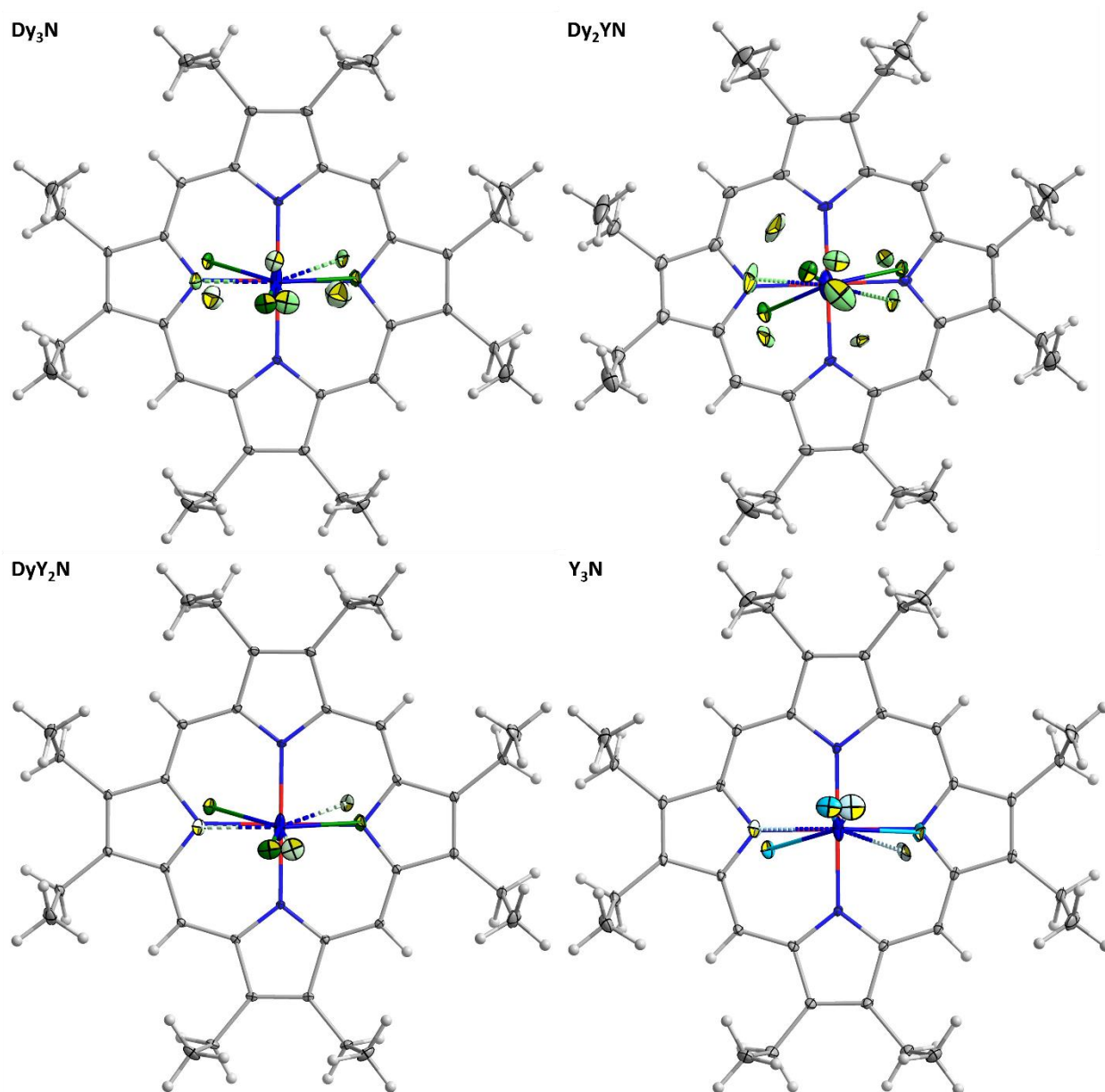
Figure S4. Orientation of endohedral M_3N (M_3N = Dy_3N, Dy_2YN, DyY_2N, and Y_3N) clusters with respect to NiOEP of $M_3N@C_{80}\cdot$NiOEP single crystals. Fullerene cage and the solvent molecules are omitted for clarity. The displacement parameters are shown at the 30% probability. Color code: grey for carbon, blue for nitrogen, white for hydrogen, red for nickel, green for dysprosium, and cyan for yttrium.

Table S3. $M_3N@I_h$-C_{80}·NiOEP (CoOEP) co-crystals.

M$_3$N, solvent	space group	cage sites	M sites[a]	N sites	N out of plane[b]	ref
Sc$_3$N, 1.5 CHCl$_3$/ 0.5 C$_6$H$_6$	$C2/m$, 4	1	0.75/0.25	1	planar	[14]
Sc$_3$N, 2 C$_6$H$_6$	$P\bar{1}$, 2	1	13 Sc: 0.48 etc	1		[15]
Y$_3$N, 2 C$_6$H$_6$	$C2/c$, 8	1	0.85/0.15	1	planar	tw
Gd$_3$N, 1.5 C$_6$H$_6$	$C2/m$, 4	0.5/0.5	0.41/0.04/0.02/ 0.02 (out of 0.5)	0.62/0.38	0.522(8)/0.46(2)	[16]
Tb$_3$N, 2 C$_6$H$_6$	$C2/c$, 8	1	0.97/0.03	0.60/0.40	0.453(4)/0.405(7)	[17]
Dy$_3$N, 2 C$_6$H$_6$	$C2/c$, 8	1	0.66/0.31/0.03	1	0.07(2) (planar)	[18]
	$C2/c$, 8	1	0.80/0.18/0.02	1	0.018(6) (planar)	tw
Ho$_3$N, 2 C$_6$H$_6$	$C2/c$, 8	1	0.84/0.16	1	0.058(9) (planar)	[19]
Er$_3$N, 2 C$_6$H$_6$	$C2/c$, 8	1	0.77/0.23	1	0.025(3) (planar)	[19]
	$C2/m$, 4	1	33 Er: 0.24 etc	1	0.049(4) (planar)	[20]
Tm$_3$N, 2 C$_6$H$_6$	$C2/c$, 8	1	0.67/0.33	1	planar	[21]
Lu$_3$N, 1.x C$_6$H$_6$	$C2/m$, 4	0.5/0.5	14 Lu: 0.37 etc	1	planar	[22]
Lu$_3$N, 2 C$_6$H$_6$	$P\bar{1}$, 2	1	0.85/0.15	1	planar	[23]
LaSc$_2$N, 2 C$_6$H$_6$	$C2/m$, 4	0.5/0.5	Sc 0.5/0.5, La 1	0.5/0.5	planar	[24]
CeSc$_2$N, 2 C$_6$H$_6$	$C2/c$, 8	1	1	1	planar	[25]
GdSc$_2$N, 2 C$_6$H$_6$	$C2/c$, 8	1	1	1	planar	[26]
TbSc$_2$N, 2 C$_6$H$_6$	$C2/m$, 4	0.5/0.5	Tb 0.38/0.07/0.05 Sc 0.30/0.10/0.10 (out of 0.5)	1	planar	[26]
DySc$_2$N, 2 C$_6$H$_6$	$C2/c$, 8	1	Dy 0.95/0.05; Sc 1	1	planar	[27]
DySc$_2$N, 0.7 C$_6$H$_6$/1.3 C$_7$H$_8$	$P\bar{1}$, 2	1	0.82/0.18	1	planar	
ErSc$_2$N, 1.5 C$_6$H$_6$/0.3 CHCl$_3$	$C2/m$, 4	0.5/0.5	0.40/0.04/0.04/ 0.02 (out of 0.5)	1	planar	[28]
VSc$_2$N, 1.67 C$_6$H$_6$/0.33 CHCl$_3$	$C2/m$, 4	0.42/0.29/ 0.29	0.6/0.4	1	planar	[29]
Gd$_2$ScN, 2 C$_6$H$_6$	$I2/a$, 8	1	0.85/0.15	1	planar	[26]
Dy$_2$ScN, 2 C$_6$H$_6$	$P\bar{1}$, 2	1	0.69/0.31	1	planar	[30]
V$_2$ScN, 2 C$_6$H$_6$	$C2/m$, 4	0.37/0.37/ 0.26	Sc: 0.5/0.5 V: 0.58/0.42	1	planar	[29]
DyGd$_2$N, 2 C$_6$H$_6$	$C2/c$, 8	1	Dy: 1; Gd: 0.86/0.14	0.58/0.42	0.46(2)/0.45(2)	[6]
DyEr$_2$N, 2 C$_6$H$_6$	$C2/c$, 8	1	0.80/0.20	1	planar	[6]
DyY$_2$N, 2 C$_6$H$_6$	$C2/c$, 8	1	0.59/0.05 (*Dy)	1	planar	tw
Dy$_2$YN, 2 C$_6$H$_6$	$P\bar{1}$, 2	1	3-4 sites, ~0.4 etc	1	planar	tw
Dy$_2$LaN, 2 C$_6$H$_6$	$C2/c$, 8	0.61/0.39	4 sites, 0.49 etc	0.70/0.30	0.619(4)/0.530(9)	tw
Ho$_2$LuN, 2 C$_6$H$_6$	$P\bar{1}$, 2	1	0.84/0.16	1	planar	[23]
CeLu$_2$N, 2C$_7$H$_8$	$P\bar{1}$, 2	1	0.65/0.15/0.10/ 0.06/0.04	0.53/0.47	0.349(8)/0.325(8)	[31]
DyErScN, CHCl$_3$	$C2/m$, 4	0.5/0.5	heavily disordered	1	planar	[32]

Notes: [a] when metals are strongly disordered, the number of metal sites is given and the highest site occupancy otherwise only site occupancies of all metal sites are listed; [b] calculated based on the three main metal sites.

Ab initio calculated ligand-field splitting

Table S4a. Ligand-field splitting for Dy^{3+} ion in $DySc_2N@C_{80}$ computed at the CASSCF/RASSI level

	E, cm^{-1}	% composition in $|m_J\rangle$ basis [a]	g-tensor:		
			g_x	g_y	g_z
KD1	0.0	99.7 $|\pm15/2\rangle$	0.000048797	0.000057979	19.838679692
KD2	355.8	97.0 $|\pm13/2\rangle$	0.001188899	0.001456091	17.169678599
KD3	665.7	89.7 $|\pm11/2\rangle$, 6.9 $|\pm9/2\rangle$	0.068510080	0.082782792	14.280293169
KD4	905.9	80.6 $|\pm9/2\rangle$, 7.6 $|\pm7/2\rangle$	0.709112734	0.891167392	11.273598377
KD5	1049.9	68.3 $|\pm7/2\rangle$, 17.2 $|\pm3/2\rangle$	3.732065167	4.194752622	8.089534531
KD6	1140.3	55.9 $|\pm5/2\rangle$, 19.8 $|\pm1/2\rangle$	2.229762052	3.791906956	10.287340198
KD7	1221.9	41.1 $|\pm3/2\rangle$, 23.6 $|\pm1/2\rangle$	1.167464358	1.619568336	14.784206957
KD8	1283.6	50.4 $|\pm1/2\rangle$, 35.5 $|\pm3/2\rangle$	0.390457677	1.275118627	18.313313804

[a] only two largest contributions exceeding 5% are listed

Table S4b. Ligand-field splitting for Dy^{3+} ion in $DyLu_2N@C_{80}$ computed at the CASSCF/RASSI level

	E, cm^{-1}	% composition in $|m_J\rangle$ basis [a]	g-tensor:		
			g_x	g_y	g_z
KD1	0.0	99.7 $|\pm15/2\rangle$	0.000057439	0.000068080	19.835068057
KD2	391.0	96.9 $|\pm13/2\rangle$	0.001181104	0.001419605	17.167343333
KD3	714.8	88.9 $|\pm11/2\rangle$, 7.6 $|\pm9/2\rangle$	0.077082459	0.093701119	14.276893586
KD4	959.6	79.0 $|\pm9/2\rangle$, 8.7 $|\pm7/2\rangle$	0.801305540	1.011303593	11.234348675
KD5	1103.8	66.7 $|\pm7/2\rangle$, 17.1 $|\pm3/2\rangle$	3.925324905	4.379663041	8.175329849
KD6	1194.0	55.4 $|\pm5/2\rangle$, 18.2 $|\pm1/2\rangle$	1.746680567	3.631094277	10.583789365
KD7	1276.2	39.4 $|\pm3/2\rangle$, 26.6 $|\pm1/2\rangle$	1.211367563	1.875583404	14.675425884
KD8	1347.8	48.7 $|\pm1/2\rangle$, 36.6 $|\pm3/2\rangle$	0.358235458	1.181230893	18.278845042

[a] only two largest contributions exceeding 5% are listed

Table S4c. Ligand-field splitting for Dy^{3+} ion in $DyY_2N@C_{80}$ computed at the CASSCF/RASSI level

	E, cm^{-1}	% composition in $|m_J\rangle$ basis [a]	g-tensor:		
			g_x	g_y	g_z
KD1	0.0	99.8 $|\pm15/2\rangle$	0.000087129	0.000102980	19.825465044
KD2	428.9	95.4 $|\pm13/2\rangle$	0.001592197	0.001819946	17.205233027
KD3	736.9	82.9 $|\pm11/2\rangle$, 12.7 $|\pm9/2\rangle$	0.090696714	0.110350806	14.305018976
KD4	971.4	70.4 $|\pm9/2\rangle$, 14.5 $|\pm7/2\rangle$	1.080836434	1.354016265	11.216318981
KD5	1109.5	66.1 $|\pm7/2\rangle$, 12.7 $|\pm3/2\rangle$	3.762120042	4.058762432	8.640300329
KD6	1205.0	64.1 $|\pm5/2\rangle$, 13.1 $|\pm1/2\rangle$	1.463583894	3.405546193	10.519101476
KD7	1287.2	49.0 $|\pm3/2\rangle$, 26.1 $|\pm1/2\rangle$	1.520186130	2.688622088	14.047848473
KD8	1380.2	56.2 $|\pm1/2\rangle$, 32.9 $|\pm3/2\rangle$	0.311906373	1.016380996	18.259690692

[a] only two largest contributions exceeding 5% are listed

Table S4d. Ligand-field splitting for Dy^{3+} ion in $DyLa_2N@C_{80}$ computed at the CASSCF/RASSI level

	E, cm^{-1}	% composition in $|m_J\rangle$ basis [a]	g-tensor:		
			g_x	g_y	g_z
KD1	0.0	99.7 $|\pm15/2\rangle$	0.000252566	0.000362489	19.755849226
KD2	489.0	94.1 $|\pm13/2\rangle$, 5.2 $|\pm11/2\rangle$	0.012765680	0.014680536	17.152509015
KD3	763.5	75.1 $|\pm11/2\rangle$, 18.5 $|\pm9/2\rangle$	0.205516148	0.238115213	14.320635946
KD4	959.8	58.0 $|\pm9/2\rangle$, 25.0 $|\pm7/2\rangle$	1.010444640	1.374718861	11.282404739
KD5	1114.6	59.9 $|\pm7/2\rangle$, 15.8 $|\pm3/2\rangle$	3.212825474	4.872462354	8.843589951
KD6	1223.6	71.8 $|\pm5/2\rangle$, 11.5 $|\pm7/2\rangle$	8.285075877	7.802033698	0.694423581
KD7	1298.5	66.9 $|\pm3/2\rangle$, 19.5 $|\pm1/2\rangle$	2.045003298	3.173212768	13.069991596
KD8	1398.7	73.3 $|\pm1/2\rangle$, 23.3 $|\pm3/2\rangle$	0.473001808	1.695893464	17.488904704

[a] only two largest contributions exceeding 5% are listed

Table S5a. Ligand-field splitting for Dy^{3+} ion (Dy1) in $Dy_2YN@C_{80}$ computed at the CASSCF/RASSI level

	E, cm^{-1}	% composition in $|m_J\rangle$ basis [a]	g-tensor:		
			g_x	g_y	g_z
KD1	0.0	99.8 $|\pm15/2\rangle$	0.000095067	0.000108013	19.819128720
KD2	423.4	95.5 $|\pm13/2\rangle$	0.001270688	0.001476918	17.196821570
KD3	735.0	83.6 $|\pm11/2\rangle$, 12.2 $|\pm9/2\rangle$	0.086875904	0.106233352	14.296019162
KD4	973.7	71.2 $|\pm9/2\rangle$, 13.9 $|\pm7/2\rangle$	1.050469410	1.340435780	11.208844403
KD5	1111.9	65.6 $|\pm7/2\rangle$, 13.9 $|\pm3/2\rangle$	3.861446084	4.041246343	8.419148757
KD6	1207.0	62.9 $|\pm5/2\rangle$, 14.1 $|\pm1/2\rangle$	1.653139676	3.323269952	10.508159835
KD7	1289.6	47.5 $|\pm3/2\rangle$, 25.7 $|\pm1/2\rangle$	1.432462995	2.413871749	14.292412541
KD8	1377.9	55.0 $|\pm1/2\rangle$, 33.4 $|\pm3/2\rangle$	0.321522078	1.047391709	18.243716858

[a] only two largest contributions exceeding 5% are listed

Table S5b. Ligand-field splitting for Dy^{3+} ion (Dy2) in $Dy_2YN@C_{80}$ computed at the CASSCF/RASSI level

	E, cm^{-1}	% composition in $|m_J\rangle$ basis [a]	g-tensor:		
			g_x	g_y	g_z
KD1	0.0	99.8 $|\pm15/2\rangle$	0.000095235	0.000109316	19.867361332
KD2	426.7	94.4 $|\pm13/2\rangle$	0.001455639	0.001675511	17.133081802
KD3	736.6	80.0 $|\pm11/2\rangle$, 14.7 $|\pm9/2\rangle$	0.089649243	0.109683358	14.238290741
KD4	973.4	66.3 $|\pm9/2\rangle$, 17.2 $|\pm7/2\rangle$	1.061706865	1.353904857	11.201524092
KD5	1111.1	62.4 $|\pm7/2\rangle$, 13.3 $|\pm3/2\rangle$	3.831284710	4.030087649	8.490817681
KD6	1206.7	63.0 $|\pm5/2\rangle$, 14.2 $|\pm1/2\rangle$	1.636076865	3.349072291	10.486348514
KD7	1289.8	50.1 $|\pm3/2\rangle$, 23.4 $|\pm1/2\rangle$	1.454087931	2.486235030	14.236628747
KD8	1381.4	57.4 $|\pm1/2\rangle$, 32.2 $|\pm3/2\rangle$	0.310653690	0.995708179	18.218497404

[a] only two largest contributions exceeding 5% are listed

Table S6a. Ligand-field splitting for Dy^{3+} ion (Dy1) in $Dy_2LaN@C_{80}$ computed at the CASSCF/RASSI level

	E, cm^{-1}	% composition in $|m_J\rangle$ basis [a]	g-tensor:		
			g_x	g_y	g_z
KD1	0.0	99.6 $|\pm15/2\rangle$	0.000307904	0.000328498	19.784955689
KD2	440.4	95.3 $|\pm13/2\rangle$	0.005947776	0.006829800	17.159290499
KD3	743.5	82.3 $|\pm11/2\rangle$, 12.8 $|\pm9/2\rangle$	0.022483908	0.038783684	14.289903987
KD4	967.0	70.8 $|\pm9/2\rangle$, 15.2 $|\pm7/2\rangle$	0.941180072	1.125964876	11.442232232
KD5	1108.8	68.3 $|\pm7/2\rangle$, 10.1 $|\pm9/2\rangle$	3.770652774	4.414660589	9.134727423
KD6	1197.3	64.7 $|\pm5/2\rangle$, 11.6 $|\pm1/2\rangle$	9.947185568	5.157816695	0.211213789
KD7	1269.9	48.5 $|\pm3/2\rangle$, 26.4 $|\pm1/2\rangle$	1.926148735	4.011647790	13.525243642
KD8	1394.5	57.2 $|\pm1/2\rangle$, 33.3 $|\pm3/2\rangle$	0.289945752	0.879189721	18.207434567

[a] only two largest contributions exceeding 5% are listed

Table S6b. Ligand-field splitting for Dy^{3+} ion (Dy2) in $Dy_2LaN@C_{80}$ computed at the CASSCF/RASSI level

	E, cm^{-1}	% composition in $|m_J\rangle$ basis [a]	g-tensor:		
			g_x	g_y	g_z
KD1	0.0	99.8 $|\pm15/2\rangle$	0.000174441	0.000226179	19.846735321
KD2	460.2	94.9 $|\pm13/2\rangle$	0.006903388	0.008291310	17.114617785
KD3	743.3	78.1 $|\pm11/2\rangle$, 17.1 $|\pm9/2\rangle$	0.091373586	0.098553760	14.246652776
KD4	953.3	61.2 $|\pm9/2\rangle$, 23.1 $|\pm7/2\rangle$	1.335970130	1.620047474	11.256977706
KD5	1102.7	57.6 $|\pm7/2\rangle$, 15.3 $|\pm5/2\rangle$	3.120096247	4.277234765	8.331887606
KD6	1207.0	59.2 $|\pm5/2\rangle$, 16.5 $|\pm1/2\rangle$	9.476498202	5.681259752	1.859846277
KD7	1300.8	58.4 $|\pm3/2\rangle$, 17.7 $|\pm5/2\rangle$	1.455445168	1.784358488	14.143198173
KD8	1382.5	69.3 $|\pm1/2\rangle$, 24.0 $|\pm3/2\rangle$	0.435116658	1.419269115	17.979415374

[a] only two largest contributions exceeding 5% are listed
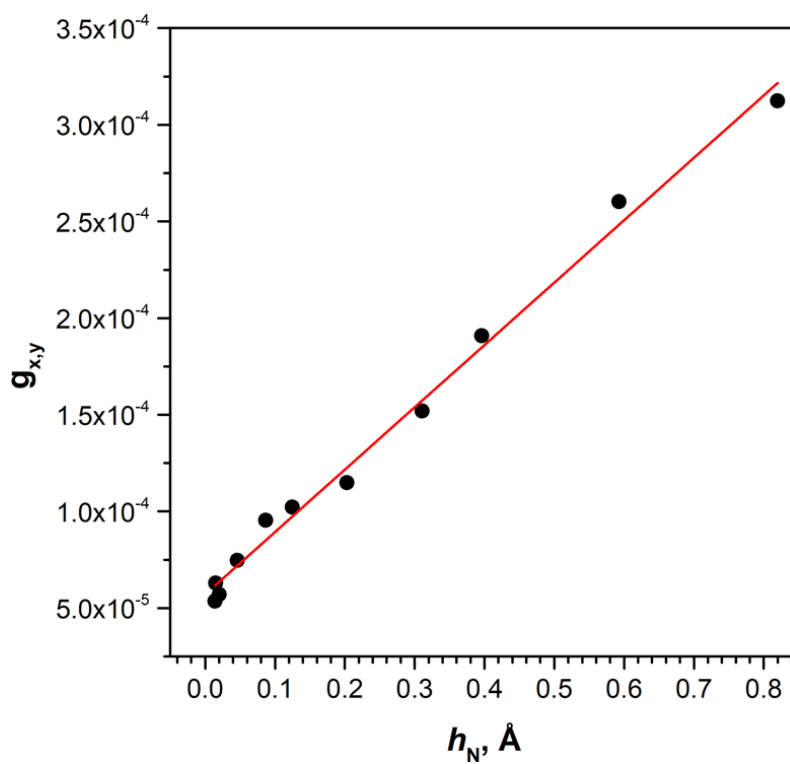
Figure S5. Correlation between $g_{x,y}$ of the ground-state KD and h_N (nitrogen out-of-plane displacement) in the series of Dy-containing $M_3N@C_{80}$ molecules (see Fig. 5 in the main text). Red line is the linear fit.

Magnetic properties
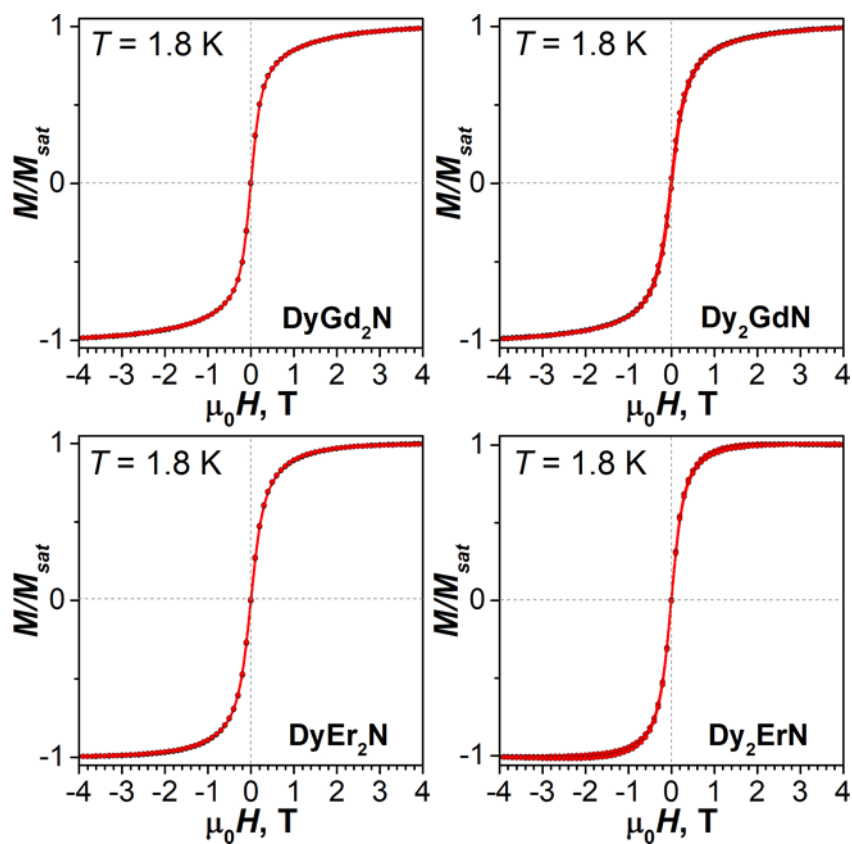
Figure S6. Magnetization curves measured for DyGd$_2$N@C$_{80}$, Dy$_2$GdN@C$_{80}$, DyEr$_2$N@C$_{80}$, and Dy$_2$ErN@C$_{80}$ at T = 1.8 K. From this group, only Dy$_2$GdN@C$_{80}$ shows narrow opening of magnetic hysteresis at 1.8 K (see Ref. [33] for a detailed study of its relaxation behavior)

Effective spin Hamiltonian

In the lowest-energy part of the spectrum, the system of two Dy ions with strong axial ligand field gives two quasi-doublets with ferromagnetic (FM) and antiferromagnetic (AFM) alignment of Dy^{3+} magnetic moments (Fig. S7). In $Dy_2MN@C_{80}$ molecule, both states have non-zero magnetic moment equal (in μ_B) $g_z \sin(\alpha/2)$ and $g_z \cos(\alpha/2)$ (where g_z is pseudospin g-tensor describing single-ion ground state, such as listed in Table S4-S6, and α is the angle between quantization axes). The state with a smaller moment is considered to be AFM, and the one with the larger moment is FM. These states can be described using the effective spin Hamiltonian as discussed in the main text:

$$\widehat{H}_{\mathrm{spin}} = \widehat{H}_{\mathrm{LF}_1} + \widehat{H}_{\mathrm{LF}_2} - 2j_{12}\widehat{J}_1 \cdot \widehat{J}_2 + \widehat{H}_{\mathrm{ZEE}} \qquad (1)$$

where $\widehat{H}_{\mathrm{LF}_i}$ are single-ion ligand-field Hamiltonians of Dy^{3+}, j_{12} is the coupling constant between dysprosium moments, and $\widehat{H}_{\mathrm{ZEE}}$ is the Zeeman term describing interaction of Dy^{3+} magnetic moments with the external magnetic field. In essence, this Hamiltonian uses single-ion ligand field ($\widehat{H}_{\mathrm{LF'}}$) terms to split Dy^{3+} multiplets into LF states (Table S4-S6), and then adds interactions between individual LF states in a bilinear form with effective constant j_{12}, which includes both exchange and dipolar interactions. We use *ab initio* computed ligand field parameters in $\widehat{H}_{\mathrm{LF}_i}$, and Dy^{3+} moments $\widehat{J}_1$ are treated in the $|J, m_j\rangle$ basis sets of the $^6H_{15/2}$ multiplet. The spectrum of the Hamiltonian also includes higher-energy states resulting from the interaction of excited LF states of single ions, but if the LF splitting is large, these states will have noticeable contribution only at high temperatures.
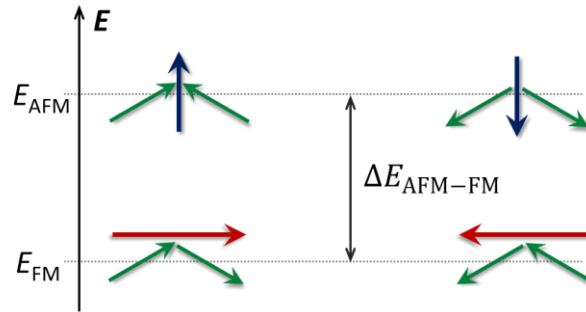

Figure S7. Schematic description of two quasi-doublets in the low-energy part of the $\{Dy_2\}$ system with Ising-type Dy^{3+} moments. Green arrows denote magnetic moments of individual Dy^{3+} ions ($\approx 10~\mu_B$ each), red and blue arrows are magnetic moments of coupled states ($\mu_{\mathrm{AFM}} = g_z \sin(\alpha/2)\mu_B$; $\mu_{\mathrm{FM}} = g_z \cos(\alpha/2)\mu_B$). The energy difference between AFM and FM states is $\Delta E_{\mathrm{AFM-FM}}$.

The Hamiltonian (1) was used in the fitting of experimental magnetization curves of $Dy_2YN@C_{80}$ and $Dy_2LaN@C_{80}$. In the fitting, j_{12} was treated as a free parameter, and computed curves were powder-averaged to be compatible with experimental magnetization curves measured for powder samples. Only experimental points in the field range where hysteresis is very narrow or completely closed were used as Hamiltonian (1) describes only magnetization in equilibrium and hence cannot be used to model magnetic hysteresis. In Fig. S8, experimental magnetization curves are compared to results of simulations with fitted parameters. The same fitted parameters were then used to simulate χT curves shown in Fig. S9.
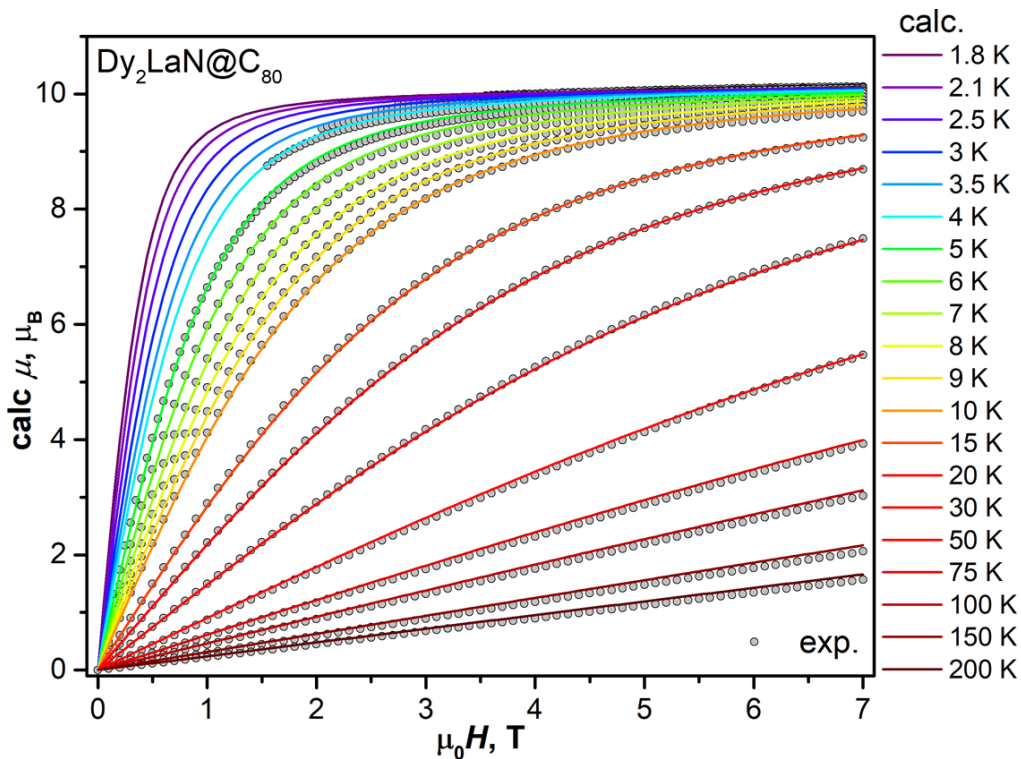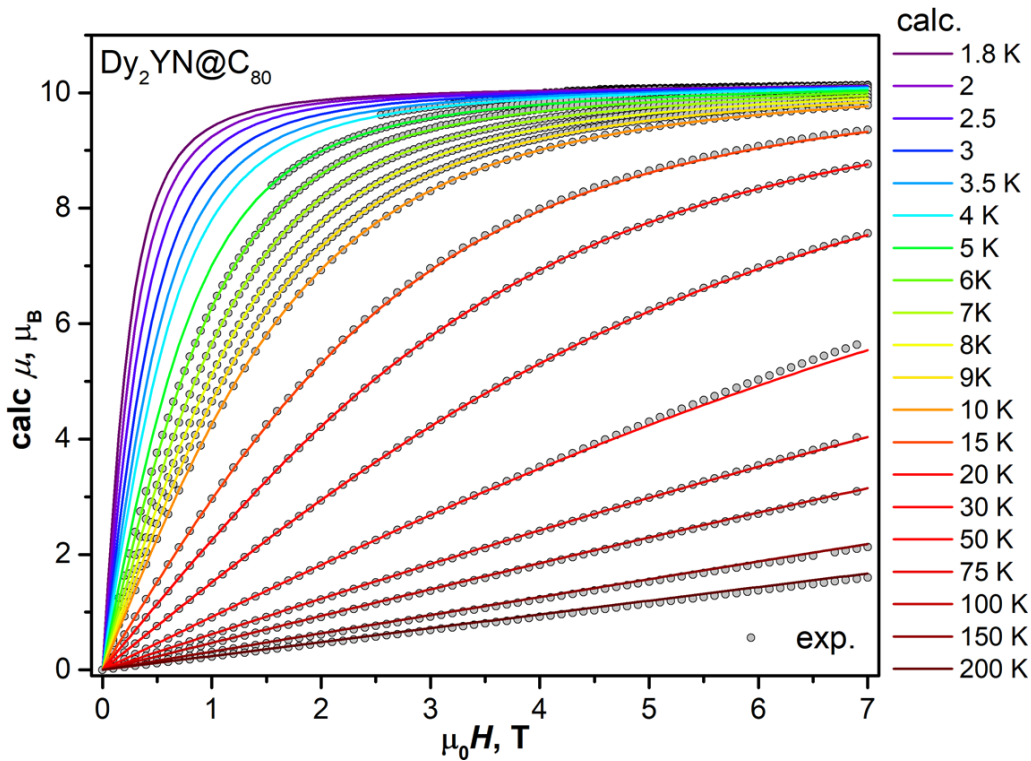
Figure S8. Experimental (dots) and fitted (colored lines) magnetization curves of $Dy_2YN@C_{80}$ (top) and $Dy_2LaN@C_{80}$ (bottom). Note that at low temperature, only high-field experimental points were used in fitting since at lower field the hysteresis was open.
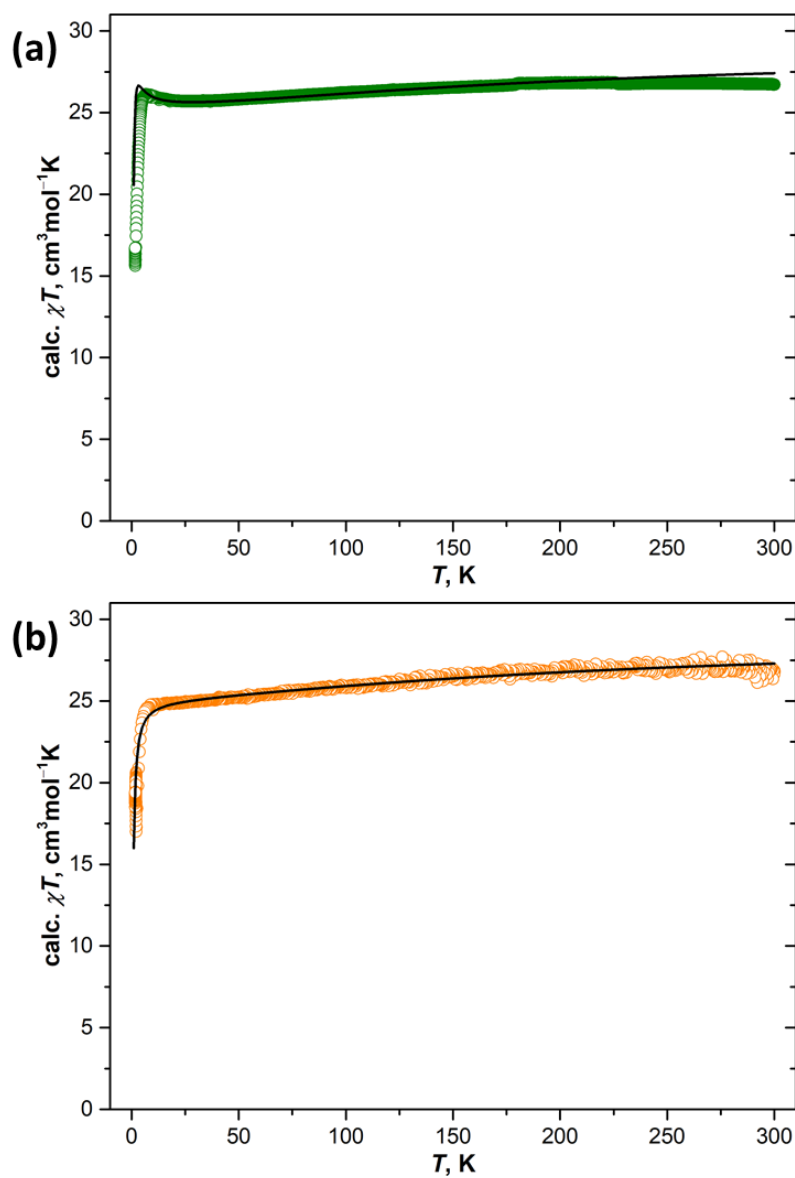
Figure S9. Experimental (dots) and simulated (black lines) χT curves of $Dy_2YN@C_{80}$ (a) and $Dy_2LaN@C_{80}$ (b), χ is defined as M/H in the field of 0.2 T. Simulations are performed with j_{12} values determined in the fit of magnetization curves.

Relaxation times

Magnetization decay curves were measured after the samples were first magnetized at 7 Tesla and then the field was quickly ramped to 0 T or 0.2 T. The decay curves were fitted with stretched exponential function:

$$M(t) = M_{eq} + (M_0 - M_{eq}) \exp\left[-\left(\frac{t}{\tau_M}\right)^\beta\right]$$

Where M_{eq} and M_0 are the equilibrium and initial magnetizations, respectively, τ_M is a characteristic relaxation time and β is a parameter, characterizing distribution of relaxation rates in the sample. For a single-exponential decay, $\beta = 1$.

In AC magnetometry studies, the in-phase and out-of-phase susceptibility, $\chi'(\nu)$ and $\chi''(\nu)$, were measured as a function of oscillation frequency ν and then fitted with the generalized Debye model:

$$\chi'(\nu) = \chi_S + (\chi_T - \chi_S)\frac{1 + (\nu\tau_M)^{1-\alpha}\sin\left(\frac{\pi\alpha}{2}\right)}{1 + 2(\nu\tau_M)^{1-\alpha}\sin\left(\frac{\pi\alpha}{2}\right) + (\nu\tau_M)^{2-2\alpha}}$$

$$\chi''(\nu) = (\chi_T - \chi_S)\frac{(\nu\tau_M)^{1-\alpha}\cos\left(\frac{\pi\alpha}{2}\right)}{1 + 2(\nu\tau_M)^{1-\alpha}\sin\left(\frac{\pi\alpha}{2}\right) + (\nu\tau_M)^{2-2\alpha}}$$

Relaxation times τ_M and parameters α determined from the fits are listed in Table S4. Fitted curves along with the measured points are shown in Fig. 6 in the main text.

Table S7a. Magnetization relaxation times (τ_M) and β parameters of DyY$_2$N@C$_{80}$ determined from DC measurements in the field of 0.2 T

T, K	τ_M, s	$\pm\tau_M$	β	$\pm\beta$
2.8	5158.6	4.8	0.72	0.000
3.0	3349.8	1.7	0.74	0.000
3.2	2288.3	1.1	0.75	0.000
3.6	1190.7	0.8	0.76	0.001
4.0	682.1	1.0	0.75	0.001
4.4	450.7	0.5	0.83	0.001
5.0	233.8	0.4	0.84	0.002
5.5	148.7	0.3	0.83	0.002
6.0	102.1	0.3	0.83	0.003
7.0	48.0	0.1	0.78	0.002
8.0	28.7	0.3	0.67	0.007

Table S7b. Magnetization relaxation times (τ_M) and β parameters of Dy$_2$YN@C$_{80}$ determined from DC measurements in the fields of 0 T and 0.2 T

	$H = 0$ T				$H = 0.2$ T			
T, K	τ_M, s	$\pm\tau_M$	β	$\pm\beta$	τ_M, s	$\pm\tau_M$	β	$\pm\beta$
1.80	1250.7	5.5	0.62	0.003	728.9	0.9	0.67	0.001
1.85	1206.6	1.0	0.59	0.001	795.6	1.5	0.75	0.002
1.90	1113.3	3.8	0.64	0.003	648.1	0.9	0.66	0.001
2.00	941.1	3.0	0.63	0.003	572.8	1.3	0.69	0.002
2.10	821.0	23.2	0.62	0.023	483.0	1.0	0.71	0.001
2.20	690.9	9.6	0.62	0.009	411.8	1.0	0.72	0.001
2.27	605.4	0.9	0.60	0.001	450.1	1.3	0.82	0.002
2.35	556.0	1.9	0.63	0.003	322.6	1.1	0.76	0.002
2.50	434.4	1.5	0.62	0.003	298.9	0.5	0.72	0.001
2.65	350.0	1.5	0.63	0.003	203.6	1.3	0.80	0.002
2.80	271.0	1.1	0.63	0.004	180.2	1.0	0.77	0.002
2.95	210.7	0.5	0.66	0.002	224.8	0.5	0.84	0.002
3.10	157.2	0.7	0.73	0.613	130.3	0.6	0.77	0.003
3.25	129.3	0.5	0.71	0.002	132.3	0.6	0.84	0.003
3.40	113.4	0.5	0.67	0.003	127.0	0.3	0.87	0.001
3.50	89.2	0.5	0.74	0.006	84.4	0.2	0.77	0.002
3.65	91.7	0.2	0.71	0.002	118.6	0.3	0.88	0.002
3.80	77.3	0.1	0.69	0.002	111.5	0.7	0.88	0.004
4.00	55.2	2.6	0.69	0.002	56.2	0.1	0.73	0.002

Table S7c. Magnetization relaxation times (τ_M) and β parameters of $Dy_2LaN@C_{80}$ determined from DC measurements in the fields of 0 T and 0.2 T

	$H = 0$ T				$H = 0.2$ T			
T, K	τ_M, s	$\pm\tau_M$	β	$\pm\beta$	τ_M, s	$\pm\tau_M$	β	$\pm\beta$
1.80	124.1	0.41	0.67	0.002	91.3	0.39	0.75	0.004
1.85	122.8	0.29	0.67	0.002	87.7	0.23	0.76	0.002
1.90	116.7	0.48	0.67	0.003	75.3	0.52	0.74	0.006
1.95	110.9	0.46	0.67	0.003	69.3	0.52	0.74	0.007
2.00	106.4	0.39	0.67	0.002	77.0	0.42	0.77	0.006
2.05	102.4	0.26	0.74	0.003	72.1	0.41	0.76	0.006
2.10	81.7	0.51	0.64	0.006	74.0	0.28	0.72	0.003
2.15	91.8	0.19	0.72	0.002	58.7	0.48	0.73	0.008
2.20	78.5	0.43	0.69	0.005	57.4	0.52	0.89	0.012
2.25	86.9	0.11	0.75	0.001	60.2	0.36	0.75	0.006
2.30	83.6	0.13	0.74	0.002	58.8	0.33	0.81	0.006
2.35	66.9	0.49	0.65	0.006	56.8	0.35	0.78	0.006
2.40	62.7	0.43	0.65	0.005	52.7	0.26	0.67	0.004
2.45	72.7	0.16	0.72	0.002	45.3	0.44	0.76	0.009
2.50	56.8	0.51	0.66	0.006	48.9	0.40	0.77	0.008

Table S8a. Magnetization relaxation times (τ_M) and α parameters of $DyY_2N@C_{80}$ determined from AC measurements in zero field

| T, K	τ_M, s	$\pm\tau_M$	α	$\pm\alpha$
5.00	1.532E+00	4.628E-02	0.25	0.006
5.56	1.434E+00	7.744E-02	0.25	0.009
6.25	1.248E+00	3.581E-02	0.25	0.006
7.14	1.164E+00	4.001E-02	0.25	0.008
8.33	8.864E-01	2.123E-02	0.23	0.007
10.00	6.978E-01	2.049E-02	0.25	0.008
11.25	5.570E-01	1.422E-02	0.21	0.009
12.86	4.261E-01	8.910E-03	0.20	0.008
15.00	2.828E-01	3.310E-03	0.18	0.005
17.30	2.025E-01	4.680E-03	0.16	0.012
20.00	1.385E-01	2.280E-03	0.15	0.009
22.22	1.155E-01	2.180E-03	0.14	0.010
25.00	8.797E-02	1.150E-03	0.13	0.007
27.27	7.208E-02	1.470E-03	0.14	0.010
30.00	5.727E-02	1.150E-03	0.10	0.012
32.31	4.830E-02	6.568E-04	0.11	0.007
35.00	4.006E-02	9.057E-04	0.09	0.013
37.33	3.276E-02	7.028E-04	0.09	0.012
40.00	2.849E-02	6.866E-04	0.08	0.014
42.35	2.509E-02	6.602E-04	0.11	0.014
45.00	2.122E-02	7.699E-04	0.08	0.022
47.37	1.815E-02	3.197E-04	0.08	0.010
50.00	1.413E-02	8.045E-04	0.09	0.033
52.38	1.287E-02	2.517E-04	0.13	0.011
55.00	1.028E-02	3.303E-04	0.16	0.018
57.39	7.530E-03	3.034E-04	0.21	0.020
60.00	5.730E-03	2.239E-04	0.22	0.019
60.00	5.770E-03	2.910E-04	0.20	0.025
61.76	4.160E-03	2.650E-04	0.26	0.029
63.64	3.520E-03	1.817E-04	0.28	0.022
65.63	2.590E-03	2.200E-04	0.28	0.034
67.74	1.590E-03	1.882E-04	0.35	0.034

Table S8b. Magnetization relaxation times (τ_M) and α parameters of $Dy_2YN@C_{80}$ determined from AC measurements in zero field

T, K	τ_M, s	$\pm\tau_M$	α	$\pm\alpha$
6.00	2.862E+00	3.357E-01	0.52	0.008
6.50	1.486E+00	1.182E-01	0.49	0.007
7.00	8.867E-01	6.237E-02	0.48	0.008
7.50	5.813E-01	2.746E-02	0.47	0.006
8.00	3.970E-01	1.409E-02	0.45	0.006
8.50	2.941E-01	9.190E-03	0.44	0.006
9.00	2.212E-01	5.920E-03	0.44	0.006
9.50	1.713E-01	4.270E-03	0.43	0.006
10.00	1.355E-01	2.870E-03	0.42	0.005
12.00	6.656E-02	1.580E-03	0.40	0.007
15.00	3.139E-02	5.383E-04	0.37	0.006
16.67	2.364E-02	5.884E-04	0.36	0.009
18.75	1.730E-02	3.985E-04	0.34	0.008
21.40	1.304E-02	2.848E-04	0.32	0.008
25.00	9.610E-03	1.789E-04	0.29	0.007
28.20	8.000E-03	1.563E-04	0.28	0.008
32.40	6.530E-03	1.546E-04	0.25	0.009
38.00	5.280E-03	7.709E-05	0.21	0.006
41.00	4.820E-03	4.888E-05	0.19	0.005
43.00	4.490E-03	4.777E-05	0.19	0.005
45.00	4.290E-03	4.485E-05	0.17	0.005
47.00	4.000E-03	3.886E-05	0.16	0.005
49.00	3.650E-03	5.289E-05	0.15	0.007
51.00	3.350E-03	5.283E-05	0.15	0.007
52.00	3.220E-03	4.996E-05	0.15	0.007
53.00	3.040E-03	7.308E-05	0.16	0.010
54.00	2.900E-03	7.552E-05	0.16	0.011
56.00	2.610E-03	1.029E-04	0.15	0.013
57.00	2.530E-03	4.590E-05	0.15	0.007
58.00	2.430E-03	5.176E-05	0.14	0.008
59.00	2.290E-03	4.461E-05	0.16	0.007
60.00	1.990E-03	3.921E-05	0.17	0.008
61.00	1.810E-03	4.527E-05	0.19	0.010
62.00	1.550E-03	3.950E-05	0.20	0.010
62.00	1.550E-03	3.950E-05	0.20	0.010
63.00	1.540E-03	5.095E-05	0.19	0.013
64.00	1.420E-03	4.996E-05	0.20	0.013
65.00	1.190E-03	3.682E-05	0.23	0.011
66.00	1.270E-03	6.231E-05	0.18	0.018
67.00	1.080E-03	8.687E-05	0.24	0.023

T, K	τ_M, s	$\pm\tau_\mathrm{M}$	α	$\pm\alpha$
68.00	9.825E-04	4.669E-05	0.22	0.016
70.00	7.997E-04	3.393E-05	0.23	0.012
71.00	7.913E-04	4.907E-05	0.23	0.015
72.00	8.895E-04	4.807E-05	0.20	0.017
73.00	6.468E-04	5.944E-05	0.25	0.019
74.00	5.847E-04	7.023E-05	0.24	0.023
75.00	8.817E-04	9.280E-05	0.13	0.029
76.00	4.820E-04	1.009E-04	0.26	0.034
77.00	4.190E-04	1.113E-04	0.28	0.038

Photoluminescence measurements
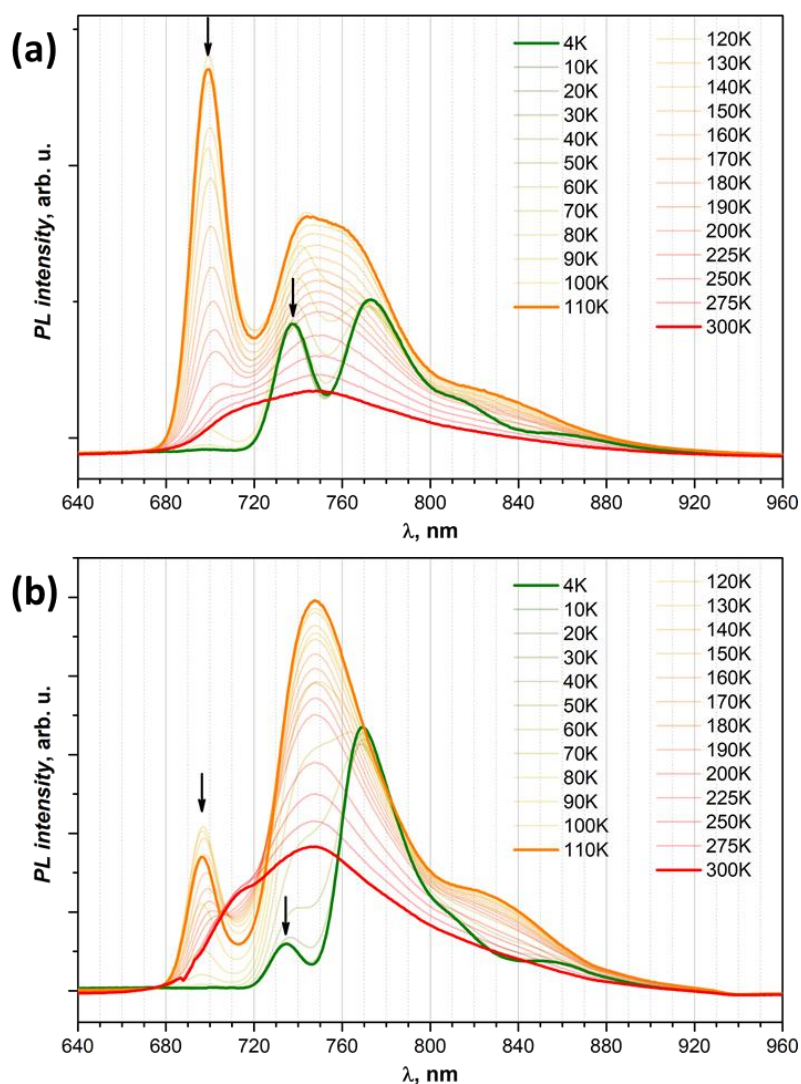
Figure S10. Variable-temperature photoluminescence measurements of $DyY_2N@C_{80}$ in polystyrene after the first separation cycle (a) and after two additional separation steps (b). Arrows denote the strongest PL lines of $Y_3N@C_{80}$ near 700 nm (fluorescence) and near 740 nm (phosphorescence). Once the PL signals of $Y_3N@C_{80}$ are reduced after three purification runs, it becomes clear that remaining PL features belong to $Y_2ScN@C_{80}$ described in Ref. [34]. Thus, there are no spectral features which can be assigned to $DyY_2N@C_{80}$, and we conclude that the compound is non-luminescent.
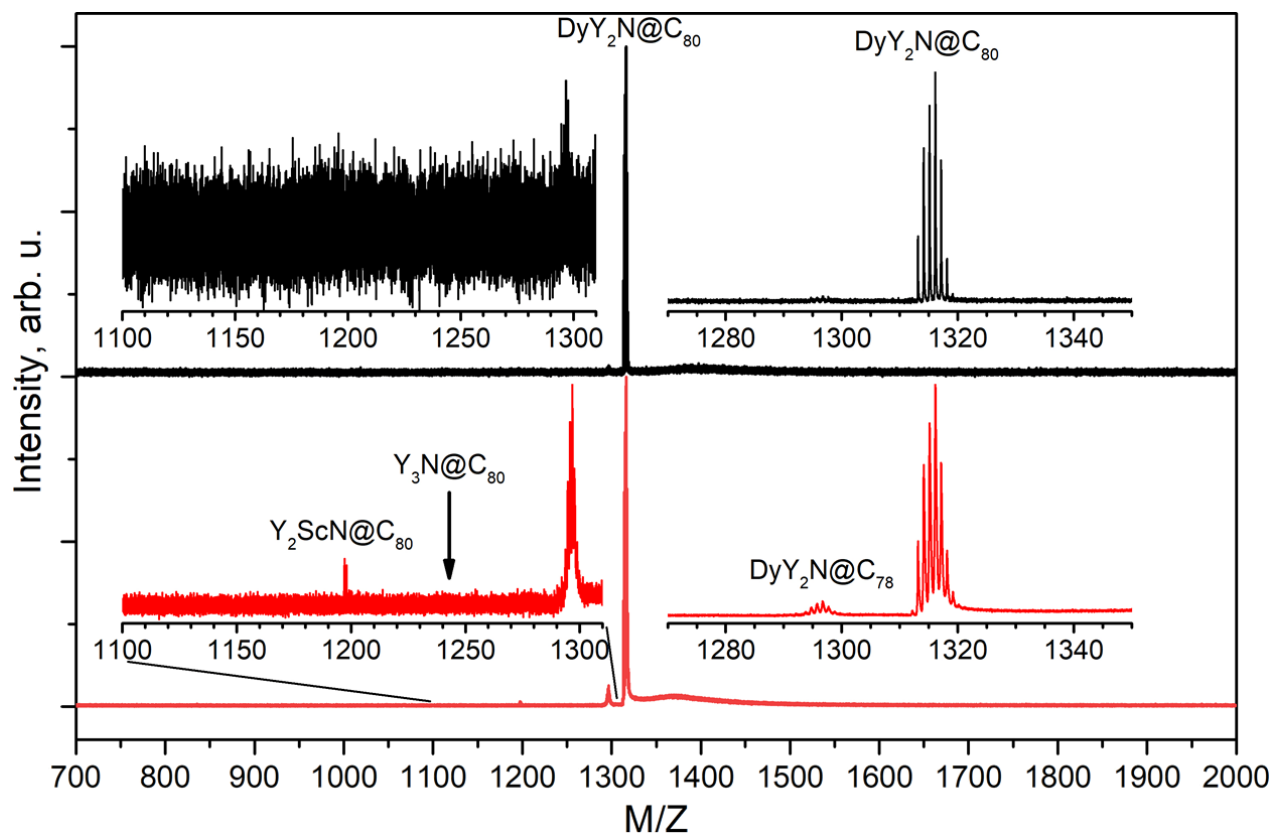
Figure S11. LDI mass spectra of $DyY_2N@C_{80}$ after 3 purification cycles (the sample, which PL spectra are shown in Fig. S10b), positive ion mode. Upper panel (black curves) shows the spectrum measured with the standard laser power; bottom panel (red curves) is the spectrum measured with the increased laser power. While $DyY_2N@C_{80}$ is the only peak detectable in normal conditions, an increase of the laser power results in the visible fragmentation of the fullerene (appearance of the peak of $DyY_2N@C_{78}$). A tiny peak of $Y_2ScN@C_{80}$ also becomes visible, whereas the signal of $Y_3N@C_{80}$ remains below detection limit of LDI-MS.

References

1.	Mueller, U.; Förster, R.; Hellmig, M.; Huschmann, F. U.; Kastner, A.; Malecki, P.; Pühringer, S.; Röwer, M.; Sparta, K.; Steffien, M.; Ühlein, M.; Wilk, P.; Weiss, M. S., The macromolecular crystallography beamlines at BESSY II of the Helmholtz-Zentrum Berlin: Current status and perspectives. *Eur. Phys. J. Plus* **2015,** *130* (7), 141.
2.	Kabsch, W., XDS. *Acta Cryst. D* **2010,** *66* (2), 125-132.
3.	Sparta, K. M.; Krug, M.; Heinemann, U.; Mueller, U.; Weiss, M. S., XDSAPP2.0. *J. Appl. Crystallogr.* **2016,** *49* (3), 1085-1092.
4.	Sheldrick, G., Crystal structure refinement with SHELXL. *Acta Cryst. C* **2015,** *71* (1), 3-8.
5.	Chilton, N. F.; Anderson, R. P.; Turner, L. D.; Soncini, A.; Murray, K. S., PHI: A powerful new program for the analysis of anisotropic monomeric and exchange-coupled polynuclear d- and f-block complexes. *J. Comput. Chem.* **2013,** *34* (13), 1164-1175.
6.	Schlesier, C.; Liu, F.; Dubrovin, V.; Spree, L.; Büchner, B.; Avdoshenko, S.; Popov, A. A., Mixed dysprosium-lanthanide nitride clusterfullerenes $DyM_2N@C_{80}$-I_h and $Dy_2MN@C_{80}$-I_h (M = Gd, Er, Tm, and Lu): synthesis, molecular structure, and quantum motion of the endohedral nitrogen atom. *Nanoscale* **2019,** *11*, 13139-13153
7.	Hafner, J., Ab-initio simulations of materials using VASP: Density-functional theory and beyond. *J. Comput. Chem.* **2008,** *29* (13), 2044-2078.
8.	Kresse, G.; Hafner, J., Ab initio molecular dynamics for liquid metals. *Phys. Rev. B* **1993,** *47* (1), 558-561.
9.	Kresse, G.; Joubert, D., From ultrasoft pseudopotentials to the projector augmented-wave method. *Phys. Rev. B* **1999,** *59* (3), 1758-1775.
10.	Perdew, J. P.; Burke, K.; Ernzerhof, M., Generalized gradient approximation made simple. *Phys. Rev. Lett.* **1996,** *77* (18), 3865-3868.
11.	Grimme, S., Density functional theory with London dispersion corrections. *WIREs Comput. Mol. Sci.* **2011,** *1* (2), 211-228.
12.	Aquilante, F.; Autschbach, J.; Baiardi, A.; Battaglia, S.; Borin, V. A.; Chibotaru, L. F.; Conti, I.; Vico, L. D.; Delcey, M.; Galván, I. F.; Ferré, N.; Freitag, L.; Garavelli, M.; Gong, X.; Knecht, S.; Larsson, E. D.; Lindh, R.; Lundberg, M.; Malmqvist, P. Å.; Nenov, A.; Norell, J.; Odelius, M.; Olivucci, M.; Pedersen, T. B.; Pedraza-González, L.; Phung, Q. M.; Pierloot, K.; Reiher, M.; Schapiro, I.; Segarra-Martí, J.; Segatta, F.; Seijo, L.; Sen, S.; Sergentu, D.-C.; Stein, C. J.; Ungur, L.; Vacher, M.; Valentini, A.; Veryazov, V., Modern quantum chemistry with [Open]Molcas. *J. Chem. Phys.* **2020,** *152* (21), 214117.
13.	Chibotaru, L. F.; Ungur, L., Ab initio calculation of anisotropic magnetic properties of complexes. I. Unique definition of pseudospin Hamiltonians and their derivation. *J. Chem. Phys.* **2012,** *137* (6), 064112.
14.	Stevenson, S.; Rice, G.; Glass, T.; Harich, K.; Cromer, F.; Jordan, M. R.; Craft, J.; Hadju, E.; Bible, R.; Olmstead, M. M.; Maitra, K.; Fisher, A. J.; Balch, A. L.; Dorn, H. C., Small-bandgap endohedral metallofullerenes in high yield and purity. *Nature* **1999,** *401* (6748), 55-57.
15.	Hao, Y.; Wang, Y.; Spree, L.; Liu, F., Rotation of fullerene molecules in the crystal lattice of fullerene/porphyrin: C_{60} and $Sc_3N@C_{80}$. *Inorg. Chem. Front.* **2021,** *8*, 122-126.
16.	Stevenson, S.; Phillips, J. P.; Reid, J. E.; Olmstead, M. M.; Rath, S. P.; Balch, A. L., Pyramidalization of Gd_3N inside a C_{80} cage. The synthesis and structure of $Gd_3N@C_{80}$. *Chem. Commun.* **2004**, (24), 2814-2815.
17.	Zuo, T. M.; Beavers, C. M.; Duchamp, J. C.; Campbell, A.; Dorn, H. C.; Olmstead, M. M.; Balch, A. L., Isolation and structural characterization of a family of endohedral fullerenes including the large, chiral cage fullerenes $Tb_3N@C_{88}$ and $Tb_3N@C_{86}$ as well as the I_h and D_{5h} isomers of $Tb_3N@C_{80}$. *J. Am. Chem. Soc.* **2007,** *129* (7), 2035-2043.

18.   Yang, S. F.; Troyanov, S. I.; Popov, A. A.; Krause, M.; Dunsch, L., Deviation from the planarity - a large Dy_3N cluster encapsulated in an I_h-C_{80} cage: An X-ray crystallographic and vibrational spectroscopic study. *J. Am. Chem. Soc.* **2006,** *128* (51), 16733-16739.

19.   Olmstead, M. M.; Zuo, T.; Dorn, H. C.; Li, T.; Balch, A. L., Metal ion size and the pyramidalization of trimetallic nitride units inside a fullerene cage: Comparisons of the crystal structures of $M_3N@I_h$-C_{80} (M = Gd, Tb, Dy, Ho, Er, Tm, Lu, and Sc) and some mixed metal counterparts. *Inorg. Chim. Acta* **2017,** *468*, 321-326.

20.   Hu, S.; Zhao, P.; Shen, W.; Yu, P.; Huang, W.; Ehara, M.; Xie, Y.; Akasaka, T.; Lu, X., Crystallographic characterization of $Er_3N@C_{2n}$ ($2n$ = 80, 82, 84, 88): the importance of a planar Er_3N cluster. *Nanoscale* **2019,** *11* (28), 13415-13422.

21.   Zuo, T.; Olmstead, M. M.; Beavers, C. M.; Balch, A. L.; Wang, G.; Yee, G. T.; Shu, C.; Xu, L.; Elliott, B.; Echegoyen, L.; Duchamp, J. C.; Dorn, H. C., Preparation and Structural Characterization of the I_h and the D_{5h} Isomers of the Endohedral Fullerenes $Tm_3N@C_{80}$: Icosahedral C_{80} Cage Encapsulation of a Trimetallic Nitride Magnetic Cluster with Three Uncoupled Tm^{3+} Ions. *Inorg. Chem.* **2008,** *47* (12), 5234-5244.

22.   Shen, W.; Bao, L. B.; Hu, S.; Gao, X.; Xie, Y.; Gao, X.; Huang, W.; Lu, X., Isolation and Crystallographic Characterization of $Lu_3N@C_{2n}$ (2n = 80-88): Cage Selection by Cluster Size. *Chem.-Eur. J.* **2018,** *24* (62), 16692-16698.

23.   Liu, F.; Spree, L., Molecular spinning top: visualizing the dynamics of $M_3N@C_{80}$ with variable temperature single crystal X-ray diffraction. *Chem. Commun.* **2019,** *55* (86), 13000-13003.

24.   Stevenson, S.; Rose, C. B.; Maslenikova, J. S.; Villarreal, J. R.; Mackey, M. A.; Mercado, B. Q.; Chen, K.; Olmstead, M. M.; Balch, A. L., Selective Synthesis, Isolation, and Crystallographic Characterization of $LaSc_2N@I_h$-C_{80}. *Inorg. Chem.* **2012,** *51* (24), 13096–13102.

25.   Wang, X. L.; Zuo, T. M.; Olmstead, M. M.; Duchamp, J. C.; Glass, T. E.; Cromer, F.; Balch, A. L.; Dorn, H. C., Preparation and structure of $CeSc_2N@C_{80}$: An icosahedral carbon cage enclosing an acentric $CeSc_2N$ unit with buried f electron spin. *J. Am. Chem. Soc.* **2006,** *128* (27), 8884-8889.

26.   Stevenson, S.; Chancellor, C.; Lee, H. M.; Olmstead, M. M.; Balch, A. L., Internal and External Factors in the Structural Organization in Cocrystals of the Mixed-Metal Endohedrals ($GdSc_2N@I_h$-C_{80}, $Gd_2ScN@I_h$-C_{80}, and $TbSc_2N@I_h$-C_{80}) and Nickel(II) Octaethylporphyrin. *Inorg. Chem.* **2008,** *47* (5), 1420-1427.

27.   Krylov, D.; Liu, F.; Brandenburg, A.; Spree, L.; Bon, V.; Kaskel, S.; Wolter, A.; Buchner, B.; Avdoshenko, S.; Popov, A. A., Magnetization relaxation in the single-ion magnet $DySc_2N@C_{80}$: quantum tunneling, magnetic dilution, and unconventional temperature dependence. *Phys. Chem. Chem. Phys.* **2018,** *20*, 11656-11672.

28.   Olmstead, M. M.; de Bettencourt-Dias, A.; Duchamp, J. C.; Stevenson, S.; Dorn, H. C.; Balch, A. L., Isolation and crystallographic characterization of $ErSc_2N@C_{80}$: an endohedral fullerene which crystallizes with remarkable internal order. *J. Am. Chem. Soc.* **2000,** *122* (49), 12220-12226.

29.   Wei, T.; Wang, S.; Lu, X.; Tan, Y.-Z.; Huang, J.; Liu, F.; Li, Q.; Xie, S.; Yang, S., Entrapping a Group-VB Transition Metal, Vanadium, within an Endohedral Metallofullerene: $V_xSc_{3-x}N@I_h$-C_{80} (x=1, 2). *J. Am. Chem. Soc.* **2016,** *138* (1), 207-14.

30.   Krylov, D. S.; Liu, F.; Avdoshenko, S. M.; Spree, L.; Weise, B.; Waske, A.; Wolter, A. U. B.; Büchner, B.; Popov, A. A., Record-high thermal barrier of the relaxation of magnetization in the nitride clusterfullerene $Dy_2ScN@C_{80}$-I_h. *Chem. Commun.* **2017,** *53*, 7901-7904.

31.   Stevenson, S.; Thompson, H. R.; Arvola, K. D.; Ghiassi, K. B.; Olmstead, M. M.; Balch, A. L., Isolation of $CeLu_2N@I_h$-C_{80} through a Non-Chromatographic, Two-Step Chemical Process and Crystallographic Characterization of the Pyramidalized $CeLu_2N$ within the Icosahedral Cage. *Chem.-Eur. J.* **2015,** *21* (29), 10362–10368.

32.   Nie, M.; Xiong, J.; Zhao, C.; Meng, H.; Zhang, K.; Han, Y.; Li, J.; Wang, B.; Feng, L.; Wang, C.; Wang, T., Luminescent single-molecule magnet of metallofullerene DyErScN@I_h-C_{80}. *Nano Res.* **2019,** *12* (7), 1727-1731.

33.   Kostanyan, A.; Schlesier, C.; Westerström, R.; Dreiser, J.; Fritz, F.; Büchner, B.; Popov, A. A.; Piamonteze, C.; Greber, T., Gadolinium as an accelerator for reaching thermal equilibrium and its influence on the ground state of $Dy_2GdN@C_{80}$ single-molecule magnets. *Phys. Rev. B* **2021,** *103* (1), 014404.

34.   Zalibera, M.; Ziegs, F.; Schiemenz, S.; Dubrovin, V.; Lubitz, W.; Savitsky, A.; Deng, S.; Wang, X.-B.; Avdoshenko, S.; Popov, A. A., Metallofullerene photoswitches driven by photoinduced fullerene-to-metal electron transfer. *Chem. Sci.* **2021,** *12*, 7818-7838.